JOURNAL OF COMPUTATIONAL PHYSICS **139,** 184–208 (1998)
ARTICLE NO. CP975855

A Reflectionless Sponge Layer Absorbing Boundary Condition for the Solution of Maxwell's Equations with High-Order Staggered Finite Difference Schemes

Peter G. Petropoulos,* Li Zhao,† and Andreas C. Cangellaris‡

*Department of Mathematics, Southern Methodist University, Dallas, Texas 75275; †Department of Electrical and Computer Engineering, University of Arizona, Tucson, Arizona 85721; ‡Department of Electrical and Computer Engineering, University of Illinois at Urbana-Champaign, Urbana, Illinois 61801
E-mail: peterp@golem.math.smu.edu, zhao@ece.arizona.edu, cangel@decwa.ece.uiuc.edu

Received November 11, 1996

We develop, implement, and demonstrate a reflectionless sponge layer for truncating computational domains in which the time-dependent Maxwell equations are discretized with high-order staggered nondissipative finite difference schemes. The well-posedness of the Cauchy problem for the sponge layer equations is proved, and the stability and accuracy of their discretization is analyzed. With numerical experiments we compare our approach to classical techniques for domain truncation that are based on second- and third-order physically accurate local approximations of the true radiation condition. These experiments indicate that our sponge layer results in a greater than three orders of magnitude reduction of the lattice truncation error over that afforded by such classical techniques. We also show that our strongly well-posed sponge layer performs as well as the ill-posed split-field Berenger PML absorbing boundary condition. Being an unsplit-field approach, our sponge layer results in ∼25% savings in computational effort over that required by a split-field approach.

1. INTRODUCTION

The analysis of electromagnetic problems involving pulsed radars and high power microwaves, the regulation of exposure of humans and electronic devices to electromagnetic

0021-9991/98 $25.00

transients, radar cross-section reduction efforts, and ground-penetrating radar modeling requires numerically solving the underlying *linear* time-domain Maxwell equations [15]

$$\begin{aligned} \frac{\partial \mathbf{B}}{\partial t} &= -\nabla \times \mathbf{E} \\ \frac{\partial \mathbf{D}}{\partial t} &= \nabla \times \mathbf{H} - \mathbf{J}, \end{aligned} \tag{1.1}$$

where $\mathbf{J}$ is an impressed current. In the absence of impressed charges the fields are divergence-free, $\nabla \cdot \mathbf{D} = 0$, $\nabla \cdot \mathbf{B} = 0$. In general, system (1.1) is closed with constitutive relations, $\mathbf{D} = \mathcal{F}[\mathbf{E}, \mathbf{H}]$ and $\mathbf{B} = \mathcal{G}[\mathbf{E}, \mathbf{H}]$, that are hereditary functionals of the electric ($\mathbf{E}$) and magnetic ($\mathbf{H}$) fields. For example, to model linear propagation of electromagnetic transients through water or biological tissue one would employ the constitutive relations $\mathbf{B} = \mu_0 \mathbf{H}$, where μ_0 is the permeability of free-space, and $\mathbf{D}(\mathbf{x}, t) = \epsilon(\mathbf{x})\mathbf{E}(\mathbf{x}, t) + \int_0^t \chi(\mathbf{x}, t - t')\mathbf{E}(\mathbf{x}, t')dt'$, where $\epsilon(\mathbf{x}) \geq \epsilon_0$ for $\mathbf{x} \in \mathcal{R}^3$ is the dielectric permittivity, ϵ_0 is the permittivity of free-space, and $\chi(\mathbf{x}, t)$ (the "memory") is the time-domain susceptibility kernel [15]. Although recent technological advances have made it necessary to consider nonlinear problems [20], the nonlinearity in these cases is introduced at the level of the constitutive relations so system (1.1) remains linear. A mini-review of computational electromagnetics (CEM) can be found in [19].

In a typical application we wish to solve for the fields everywhere inside the computational box depicted in Fig. 1 for a given incident signal. A very successful numerical approach

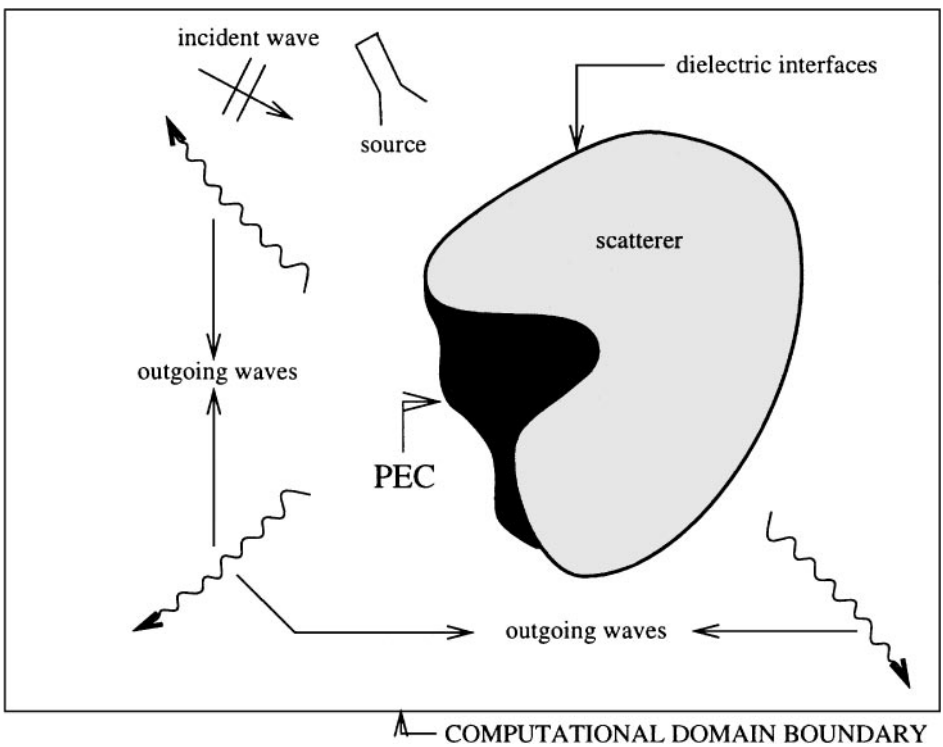

FIG. 1. The computational domain is embedded in free-space.

is the finite-difference time-domain method (FD-TD, also known as the Yee-scheme [28]). A good review of the method and of a host of applications can be found in [25]. The FD-TD method is a nondissipative second-order accurate finite difference scheme in which the field unknowns are staggered in space-time. In fact [18], it is the **best** second-order accurate scheme for the time-dependent Maxwell equations that preserves the divergence-free property of **D** and **B**, and many radiation/absorbing boundary conditions (RBC/ABCs) have been developed to truncate FD-TD lattices. Staggering the unknowns in space-time also results in more efficiency [10]. However, electrically large electromagnetic problems and the need to increase the predictive dynamic range [25] of CEM modeling codes while retaining the capability to do the computation with existing computational resources, call for numerical schemes with an order of accuracy greater than two. High-order accuracy is also called for when use of realistic models of materials is made; our previous work [22] explored this issue for the Yee-scheme and suggested that staggered nondissipative schemes of $O(\Delta t^2)+O(\Delta^4)$ accuracy [6], where Δ is the cell size in each spatial coordinate direction and Δt is the timestep, are more natural for such problems. Additionally, taking into account the amount of arithmetic operations per timestep and using the results in [21] we can estimate the computational cost of the (2, 4) relative to the Yee-scheme for two-dimensional problems as $C^{rel} \approx 1.16 \times (\nu^{22}/\nu^{24})(e_\phi^{\text{tot}}/L)^{3/4}$, where ν^{22} and ν^{24} are the respective CFL numbers, e_ϕ^{tot} is the total phase error allowed to accumulate, and L is the computational domain size w.r.t. smallest wavelength in the problem. For a fixed Δ, the (2, 4) scheme should be used with $\nu^{24} \approx 0.1 \times \nu^{22}$ to balance the time and space errors. However, the (2, 4) is still much cheaper than the Yee-scheme for electrically large problems and high accuracy.

Unfortunately, high-order schemes have not been accepted by the engineering CEM community. One reason for this is the wider stencil of these methods that does not allow for a straightforward implementation of the absorbing boundary conditions [7] needed to simulate the fact that the problem to be solved is embedded in free-space. Previous attempts with conventional sponge layers [14, 17] and image methods [4, 5] do not appear to have been as successful as required in order for them to become popular for high-order stencils. On the other hand, one-dimensional local radiation boundary conditions [13] are easy to implement with high-order stencils.

In this paper we address the radiation boundary condition issue for high-order staggered stencils. In Section 3 a reflectionless sponge layer is developed in rectangular coordinates; it is invisible to propagating waves impinging on it and is used for the purpose of absorbing such waves as they exit a computational domain. The derivation allows us to produce, using the inverse Fourier transform, time-domain equations that we discretize and use as an absorbing boundary condition for the (2, 4) staggered scheme which is briefly described in Section 2. We show that our sponge layer equations form a strongly well-posed system as all the necessary extra terms are lower-order with respect to the principal part of Maxwell's equations. Contrary to the standard radiation conditions, the sponge layer herein does not alter the local nature of the interior scheme and makes irrelevant the boundary condition (BC) used on the last set of nodes on the computational boundary; we implement a perfect electric conductor (PEC) condition on these nodes; i.e., the tangential fields satisfy a homogeneous Dirichlet boundary condition. We also show that the discrete sponge layer is stable under the necessary and sufficient stability condition of the interior scheme. Numerical scattering experiments, designed to isolate and study the error introduced by the sponge layer, are presented in Section 4. There, mesh refinement studies indicate the superiority of the sponge layer. A summary closes the paper in Section 5.

Significantly, our sponge layer preserves all the desirable properties of the popular Berenger boundary condition while possessing none of its undesirable mathematical properties. Berenger [2] introduced an electrically and magnetically lossy, perfectly matched layer (PML) by altering the principal part of Maxwell's equations in order to introduce anisotropy. In two dimensions (TM-polarization) his equations in the layer are no longer the familiar 3×3 hyperbolic system with lower-order electric and magnetic loss terms. Rather, the equations now form a 4×4 system through an arbitrary splitting of the scalar field component. Casting the Berenger system in the form $\mathbf{u}_t = A\mathbf{u}_x + B\mathbf{u}_z + C\mathbf{u}$, where $\mathbf{u} = (H_x, H_z, H_{yx}, E_{yz})^T$, allows for a crucial observation as shown in [1]. The 4×4 matrices A and B are not simultaneously symmetrizable; the system is weakly hyperbolic, and standard analysis then leads to proving that the Cauchy problem for the principal part of the Berenger equations is weakly well-posed and becomes ill-posed under perturbation by lower order terms (such as the ones needed to damp the waves entering the PML). Consequently, and centered-difference scheme (such as (2.3) below) is bound to be unconditionally unstable [1] when used in conjunction with Berenger's equations. In Section 4 we show our sponge layer results are comparable to those obtained using the Berenger layer; thus, our method is superior in light of the desirability of strongly well-posed problems for numerical work. Additionally, we show in Section 4 that the unsplit-field implementation of our sponge layer results in memory savings of $\sim$25% over Berenger's split-field PML.

We must note here that [16] derived and demonstrated a reflectionless sponge layer for two-dimensional acoustics; the relationship of our approach to that of [16] is described in Section 3a. Also, some global radiation boundary conditions [8, 9] have been developed for scalar hyperbolic problems. Their expected performance should be, at least, similar to that of the local reflectionless sponge layer presented herein. Unfortunately, [8] is unstable when used with nondissipative schemes, while [9] works only in spherical coordinates. An open problem is whether other global radiation conditions [12, 27] developed for fluid flow problems can be adapted for CEM.

2. INTERIOR SCHEME

a. *Model Equations*

Setting $\mathbf{D} = \hat{y} D_y = \hat{y}\epsilon E_y$, $\mathbf{B} = \mu\mathbf{H} = \mu(\hat{x} H_x + \hat{z} H_z)$ in (1.1) we consider the transverse magnetic (TM) polarization case inside a computational domain. The model equations are

$$\begin{aligned} \mu \frac{\partial H_x}{\partial t} &= \frac{\partial E_y}{\partial z} \\ \mu \frac{\partial H_z}{\partial t} &= -\frac{\partial E_y}{\partial x} \\ \epsilon \frac{\partial E_y}{\partial t} &= -\frac{\partial H_z}{\partial x} + \frac{\partial H_x}{\partial z}. \end{aligned} \tag{2.1}$$

The two-dimensional system (2.1) can be cast in the form $\mathbf{u}_t + A\mathbf{u}_x + B\mathbf{u}_z = 0$, where $\mathbf{u} = (H_x, H_z, E_y)^T$, and

$$A = \begin{pmatrix} 0 & 0 & 0 \\ 0 & 0 & 1/\mu \\ 0 & 1/\epsilon & 0 \end{pmatrix}, \qquad B = \begin{pmatrix} 0 & 0 & -1/\mu \\ 0 & 0 & 0 \\ -1/\epsilon & 0 & 0 \end{pmatrix}. \tag{2.2}$$

By Definition 6.3.1 of [11] system (2.1) is symmetric hyperbolic; A and B each have three distinct real eigenvalues, a complete set of eigenvectors, and are simultaneously symmetrizable (the diagonalizer P of A leaves PBP^{-1} symmetric). Consequently, it is strongly hyperbolic and the matrix $\omega_1 A + \omega_2 B$ is diagonalizable by $S(\omega_1, \omega_2)$ for any real ω_1, ω_2 satisfying $|\omega_1|^2 + |\omega_2|^2 = 1$. Further, the diagonalizer S and its inverse, S^{-1}, are bounded independent of ω_1, ω_2. It follows that system (2.1) is **strongly well-posed** (Theorem 6.3.2 in [11]).

b. *Model Discretization and Stability*

The discrete fields $(HX, HZ, EY)^T$ are staggered on a cartesian $x - z$ grid of equal cell size, Δ, in both coordinate directions. Staggering the HX, HZ, and EY fields in time results in the differenced version of (2.1),

$$\begin{aligned}
\mu \frac{HX^{n+1/2}_{i,j+1/2} - HX^{n-1/2}_{i,j+1/2}}{\Delta t} &= \delta^z(\alpha, \beta) EY^n_{(i,j+1/2)} \\
\mu \frac{HZ^{n+1/2}_{i+1/2,j} - HZ^{n-1/2}_{i+1/2,j}}{\Delta t} &= -\delta^x(\alpha, \beta) EY^n_{(i+1/2,j)} \\
\epsilon \frac{EY^{n+1}_{i,j} - EY^n_{i,j}}{\Delta t} &= -\delta^x(\alpha, \beta) HZ^{n+1/2}_{(i,j)} + \delta^z(\alpha, \beta) HX^{n+1/2}_{(i,j)}.
\end{aligned} \tag{2.3}$$

Parenthesized subscripts in (2.3) denote the spatial location where the discrete derivative of the field variable is to be calculated, while subscripts without parentheses denote the actual grid location of the relevant field variable. The discrete spatial derivatives are calculated via

$$\partial_{x(z)} \approx \delta^{x(z)}(\alpha, \beta) = \frac{1}{\Delta}\left[\alpha\left(S^{1/2}_{x(z)} - S^{-1/2}_{x(z)}\right) + \beta\left(S^{3/2}_{x(z)} - S^{-3/2}_{x(z)}\right)\right], \tag{2.4}$$

where the spatial shift operator is defined by its action $S^\ell f_{(i)} = f_{i+\ell}$, and its subscript $x(z)$ indicates on which of the two spatial indices of the discrete fields it operates. The weights, α and β, determine the order of accuracy of the scheme, i.e.,

$$\begin{aligned}
\alpha = 1, \quad \beta = 0 &\rightarrow O(\Delta t^2) + O(\Delta^2) \\
\alpha = 9/8, \quad \beta = -1/24 &\rightarrow O(\Delta t^2) + O(\Delta^4).
\end{aligned} \tag{2.5}$$

A standard stability analysis, which entails finding the relationship that ensures none of the eigenvalues of the amplification matrix Q of (2.3) are outside the unit circle, produces the necessary stability condition

$$\nu \leq \frac{1}{(\alpha - \beta)\sqrt{2}}, \tag{2.6}$$

where $\nu = c\Delta t/\Delta$ is the CFL number set with respect to the wavefront speed $c\ (= 1/\sqrt{\epsilon\mu})$ which is always the fastest speed in any given dielectric. When (2.6) is met, the amplification matrix is said to satisfy the von Neumann condition. Because (2.1) is strongly hyperbolic, the matrix S that diagonalizes $\omega_1 A + \omega_2 B$ also diagonalizes Q, i.e., $H = SQS^{-1}$. It is easy to check that $H\overline{H}^T = I$ when the von Neumann condition is satisfied, so by Theorem 6.2.5(*ii*) of [26] restriction (2.6) is **necessary and sufficient**.

c. *Radiation Boundary Conditions for Model Scheme*

To solve scattering problems embedded in an unbounded region one needs effective RBC/ABCs imposed at the boundary of the finite-sized computational domain; a multitude of such conditions has been derived [7] and are applied to the tangential fields.

The longer stencil of the (2, 4) scheme allows (2.3) to be brought up to a distance of $3\Delta/2$ away from the tangential to the boundary field variable which is to be updated with a local RBC. As a result, numerical boundary procedures are needed to update two additional tangential field nodes, one electric and one magnetic, interior to the tangential electric field boundary node. A solution to this problem can be effected using the popular local condition [13]

$$B_m\left(\frac{\partial}{\partial n}, \frac{\partial}{\partial t}\right) U = \prod_{j=1}^{m} \left(\cos\theta_j^{abs} \frac{\partial}{\partial t} - c\frac{\partial}{\partial n}\right) U = 0, \tag{2.7}$$

where m is the order of "physical" accuracy, $\pm\theta_j^{abs}$ are the angles of perfect absorption, U is a tangential (electric or magnetic) field variable at the boundary, and $\partial/\partial n$ is the spatial derivative in the outward normal direction to the computational domain boundary. The situation is depicted in Fig. 2; the nodes we deal with are to the right of the vertical dashed line. Assuming that the electric field everywhere is known at time level n and the magnetic field at time level $n - 1/2$, the scheme that includes the treatment of all the nodes on the vertical right-hand computational boundary and produces updated field variables at all locations (including the "ghost" nodes) is as follows: update HZ with (2.3) up to node $(N + \frac{1}{2}, j)$ and impose $B_m HZ^{n+1/2}_{N+3/2,\,j} = 0$ to obtain $HZ^{n+1/2}_{N+3/2,\,j}$; update HX everywhere with (2.3); update EY with (2.3) up to node (N, j) and impose $B_m EY^{n+1}_{N+1,\,j} = 0$ to obtain $EY^{n+1}_{N+1,\,j}$; impose $B_m EY^{n+1}_{N+2,\,j} = 0$ to obtain $EY^{n+1}_{N+2,\,j}$. This scheme is possible because the operator B_m (for $m = 2, 3$), when applied to, e.g., a tangential electric field variable, involves the node $i = \zeta$ (here $\zeta = N$) at time level $n + 1$, the nodes $i \le \zeta$ at time levels $\le n$, and the nodes $i \le \zeta - 1$ at the $(n + 1)$th time level. To compute the update of the magnetic ghost node and to implement the radiation condition at a horizontal computational boundary the

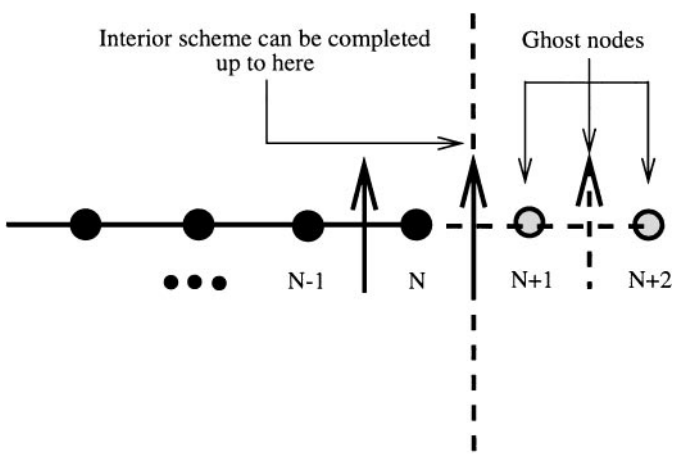

FIG. 2. The (2, 4) staggered grid along the normal to the computational domain boundary.

procedure described above is repeated, with the appropriate changes in the tangential fields and discrete spatial indices. The one-dimensional nature of the operators (2.7) allows for easy implementation at a corner where the horizontal and vertical portions of the boundary meet. Simply apply the procedure in the vertical direction up to the node $j = jmax - 1$ next to the corner node, and then use the procedure applied in the horizontal direction for all nodes i including the corner node at $j = jmax$. We will see Section 4 that the above procedure works reasonably well for transient problems.

3. THE REFLECTIONLESS SPONGE LAYER

a. *Motivation*

An alternative to radiation boundary conditions for absorbing outgoing waves involves surrounding the computational domain depicted in Fig. 1 with a wave-absorbing layer of thickness d. Ideally, the transition from the interior to the absorbing layer should not produce wave reflection while the fields that have penetrated into the layer should attenuate as they propagate outward.

Consider the one-dimensional Maxwell system for $(x, t) \in (-\infty, \infty) \times [0, \infty)$,

$$\begin{aligned} \mu \frac{\partial H}{\partial t} + \sigma^* H &= -\frac{\partial E}{\partial x} \\ \epsilon \frac{\partial E}{\partial t} + \sigma E &= -\frac{\partial H}{\partial x}, \end{aligned} \tag{3.1}$$

where $\sigma = \sigma^* = 0$ for $x < 0$ and $\sigma, \sigma^* > 0$ for $x \geq 0$. System (3.1) models an electrically and magnetically lossy "material" (occupying $x \geq 0$) with constant wavefront speed $c_\infty = 1/\sqrt{\epsilon\mu}$, placed adjacent to free-space ($x < 0$) with wavefront speed $c = 1/\sqrt{\epsilon_0\mu_0}$ ($c_\infty \leq c$). Using the notation $t_c = \epsilon/\sigma$ and $t_c^* = \mu/\sigma^*$, we compute the dispersion relation relevant to boundary value problems ($\omega \in \mathcal{R}$) in $x > 0$. For a mode $e^{i(\omega t - kx)}$ it is

$$-\omega^2 + i\frac{\omega}{t_c} + i\frac{\omega}{t_c^*} + \frac{1}{t_c t_c^*} + c_\infty^2 k^2 = 0, \tag{3.2}$$

where k is the wavenumber. Upon choosing "material" properties so that $t_c = t_c^*$ (the "PML condition") (3.2) reduces to $ik = \pm(1/c_\infty)(i\omega + 1/t_c)$; i.e., left/right moving waves in this "material" travel slower than they do in $x < 0$ and decay exponentially in space at a rate that is independent of the frequency ω. Further, if $\sqrt{\epsilon_0/\mu_0} = \sqrt{\epsilon/\mu}$ then (3.1), written as $\mathbf{u}_t + A\mathbf{u}_x + C\mathbf{u} = 0$, where $\mathbf{u} = (H, E)^T$, exhibits the following properties: $A = R\Lambda R^{-1}$ and $C = RDR^{-1}$, where $\Lambda = \text{diag}\{-c_\infty, c_\infty\}$, $D = \text{diag}\{1/c_\infty t_c, -1/c_\infty t_c\}$, and R is the diagonalizer of the A in the region $x < 0$ where the system is $u_t + Au_x = 0$; i.e., $\Lambda_{x<0} = \text{diag}\{-c, c\} = R^{-1}AR$. The eigenvectors of A are preserved across $x = 0$ while its eigenvalues are reduced; the interface at $x = 0$ will be reflectionless for any propagating wave impinging upon it from the left. The waves entering this "material" will be slowed down ($c_\infty < c$) and damped independently of frequency. The region $x \geq 0$ can be terminated at $x = d > 0$ with any BC, e.g., PEC, and the combination used as an absorbing boundary in a code that solves scattering problems in $x < 0$. Appropriately setting d, t_c, and c_∞ can, in principle, make the boundary condition at $x = d$ invisible to waves in the interior $x < 0$, as any outgoing wave of amplitude E_0 that has entered the layer, and subsequently has

reflected from the BC at $x = d$, will be further attenuated while propagating back towards $x = 0$ to re-enter the computational domain with amplitude $\sim E_0 e^{-2d/c_\infty t_c}$. We note here that the order of accuracy and stability of the interior scheme is maintained in the layer, since only time-centered lower-order terms are used to implement it.

This one-dimensional case is the only point of contact of our approach with that in [16]. Our generalization to two and three dimensions involves nonlocal in time lower-order terms and is shown below to maintain the reflectionless absorbing property of (3.1) for **all** angles of incidence. The approach in [16] involves local in time lower-order terms and the reflectionless property holds only along a "preferred" propagation direction that has to be identified during the course of the numerical solution.

b. *Derivation*

We proceed with a review of the fundamental steps in the derivation of our sponge layer in three dimensions. In this way the two-dimensional TE (scalar magnetic field) and TM (scalar electric field) polarizations will be simultaneously treated. A more detailed presentation can be found in [29]. A Fourier transform in time ($e^{i\omega t}$ dependence) and the frequency-domain anisotropic constitutive relations $\mathbf{D} = \bar{\epsilon} \cdot \mathbf{E}$ and $\mathbf{B} = \bar{\mu} \cdot \mathbf{H}$ reduce (1.1) (with $\mathbf{J} = 0$) and the divergence-free conditions to

$$\begin{aligned} i\omega\bar{\mu} \cdot \mathbf{H} &= -\nabla \times \mathbf{E} \\ i\omega\bar{\epsilon} \cdot \mathbf{E} &= \nabla \times \mathbf{H} \\ \nabla \cdot (\bar{\epsilon} \cdot \mathbf{E}) &= 0 \\ \nabla \cdot (\bar{\mu} \cdot \mathbf{H}) &= 0, \end{aligned} \tag{3.3}$$

where $\bar{\mu}, \bar{\epsilon}$, are the permeability and permittivity tensors of the medium here assumed [24] to be of the form

$$\begin{aligned} \bar{\epsilon} &= \epsilon(\mathrm{diag}\{a_x, a_y, a_z\}) = \epsilon[\Lambda] \\ \bar{\mu} &= \mu(\mathrm{diag}\{a_x, a_y, a_z\}) = \mu[\Lambda], \end{aligned} \tag{3.4}$$

with ϵ and μ being real numbers that satisfy $\epsilon \geq \epsilon_0$ and $\mu \geq \mu_0$. In (3.4), the elements of the diagonal matrix

$$[\Lambda] = \mathrm{diag}\{a_x, a_y, a_z\} \tag{3.5}$$

are, in general, complex dimensionless constants.

Next, scaled fields are introduced as

$$\begin{aligned} \hat{\mathbf{E}} &= \{\hat{E}_x, \hat{E}_y, \hat{E}_z\}^T = [G]^{-1}\{E_x, E_y, E_z\}^T \\ \hat{\mathbf{H}} &= \{\hat{H}_x, \hat{H}_y, \hat{H}_z\}^T = [G]^{-1}\{H_x, H_y, H_z\}^T, \end{aligned} \tag{3.6}$$

and

$$[G] = \mathrm{diag}\{g_x, g_y, g_z\} \tag{3.7}$$

with g_x, g_y, g_z being, in general, complex constants. Using the notation $\bar{\bar{G}}$ and $\bar{\bar{\Lambda}}$ to denote the tensors with matrix representations $[G]$ and $[\Lambda]$, respectively, we rewrite (3.3) in terms of the scaled fields,

$$\begin{aligned} i\omega\mu\,\bar{\bar{\Lambda}}\cdot\bar{\bar{\mathbf{G}}}\cdot\hat{\mathbf{H}} &= -\nabla\times(\bar{\bar{\mathbf{G}}}\cdot\hat{\mathbf{E}}) \\ i\omega\epsilon\,\bar{\bar{\Lambda}}\cdot\bar{\bar{\mathbf{G}}}\cdot\hat{\mathbf{E}} &= \nabla\times(\bar{\bar{\mathbf{G}}}\cdot\hat{\mathbf{H}}) \\ \nabla\cdot(\epsilon\,\bar{\bar{\Lambda}}\cdot\bar{\bar{\mathbf{G}}}\cdot\hat{\mathbf{E}}) &= 0 \\ \nabla\cdot(\mu\,\bar{\bar{\Lambda}}\cdot\bar{\bar{\mathbf{G}}}\cdot\hat{\mathbf{H}}) &= 0. \end{aligned} \tag{3.8}$$

The choice of the scaling factors, g_x, g_y, g_z, according to the equations

$$\left(\frac{g_x}{g_y}\right)^2=\frac{a_y}{a_z},\quad \left(\frac{g_y}{g_z}\right)^2=\frac{a_z}{a_y},\quad \left(\frac{g_z}{g_x}\right)^2=\frac{a_x}{a_z} \tag{3.9}$$

allows us to cast (3.8) in the form

$$\begin{aligned} i\omega\mu\hat{\mathbf{H}} &= -\nabla_{\mathbf{a}}\times\hat{\mathbf{E}} \\ i\omega\epsilon\hat{\mathbf{E}} &= \nabla_{\mathbf{a}}\times\hat{\mathbf{H}} \\ \nabla_{\mathbf{a}}\cdot(\epsilon\hat{\mathbf{E}}) &= 0 \\ \nabla_{\mathbf{a}}\cdot(\mu\hat{\mathbf{H}}) &= 0, \end{aligned} \tag{3.10}$$

where $\nabla_a \stackrel{\text{def}}{=} \hat{\mathbf{x}}(1/\sqrt{a_y a_z})\partial_x + \hat{\mathbf{y}}(1/\sqrt{a_x a_z})\partial_y + \hat{\mathbf{z}}(1/\sqrt{a_x a_y})\partial_z$. The system (3.10) is reminiscent of the modified Maxwell system with complex coordinate stretching used in [3]. Indeed, using the notation

$$s_x=\sqrt{a_y a_z},\quad s_y=\sqrt{a_x a_z},\quad s_z=\sqrt{a_x a_y}, \tag{3.11}$$

(3.10) becomes mathematically equivalent to the modified, frequency-domain, Maxwell system in [3]. However, there is an important difference: the system in (3.10) is for the scaled fields while the equivalent one in [3] was proposed assuming that the fields are physical fields. The nonphysicality of the fields in [3] manifests itself as the requirement for an arbitrary field-splitting in order to produce the time-domain equations for the absorbing layer.

Assuming plane wave propagation behavior for the scaled fields in the anisotropic medium

$$\begin{aligned} \hat{\mathbf{E}} &= \bar{\bar{\mathbf{G}}}^{-1}\cdot\mathbf{E}=\hat{\mathbf{E}}_0\exp(-i\mathbf{k}\cdot\mathbf{r}) \\ \hat{\mathbf{H}} &= \bar{\bar{\mathbf{G}}}^{-1}\cdot\mathbf{H}=\hat{\mathbf{H}}_0\exp(-i\mathbf{k}\cdot\mathbf{r}), \end{aligned} \tag{3.12}$$

where $\mathbf{k}=\hat{x}k_x+\hat{y}k_y+\hat{z}k_z$, and $\hat{\mathbf{E}}_0$, $\hat{\mathbf{H}}_0$ are the scaled complex-constant field amplitudes, the dispersion relation, easily obtained from (3.10) as

$$\omega^2\mu\epsilon=\frac{k_x^2}{s_x^2}+\frac{k_y^2}{s_y^2}+\frac{k_z^2}{s_z^2}, \tag{3.13}$$

is satisfied by

$$\begin{aligned} k_x &= k s_x \sin\theta \cos\phi \\ k_y &= k s_y \sin\theta \sin\phi \\ k_z &= k s_z \cos\theta, \end{aligned} \tag{3.14}$$

where $k = \omega\sqrt{\mu\epsilon}$. Clearly, the propagation characteristics of the wave along $\hat{x}$, $\hat{y}$, and $\hat{z}$ can be controlled by varying s_x, s_y, and s_z or, effectively (in view of (3.11)), by varying the properties of the anisotropic medium.

c. *Reflection Properties*

A relationship between the tensors of two anisotropic media separated by a planar interface can be established for the interface to be reflectionless for all frequencies and all angles of incidence (except grazing). This relationship is given in the following without proof. The interested reader may consult [29] for the details.

Without loss of generality the planar interface is taken to coincide with the $z = 0$ plane in a cartesian coordinate system. The space $z < 0$ (Medium 1) is filled with a homogeneous medium with tensors $\epsilon_1[\Lambda_1]$, $\mu_1[\Lambda_1]$, where $[\Lambda_1] = \text{diag}\{a_{1x}, a_{1y}, a_{1z}\}$, and corresponding s_{1x}, s_{1y}, and s_{1z} values given by (3.11). The space $z > 0$ (Medium 2) is filled with a homogeneous medium with tensors $\epsilon_2[\Lambda_2]$, $\mu_2[\Lambda_2]$, where $[\Lambda_2] = \text{diag}\{a_{2x}, a_{2y}, a_{2z}\}$, and corresponding s_{2x}, s_{2y}, and s_{2z} values given by (3.11). A plane wave propagating from Medium 1 toward Medium 2 is assumed to be obliquely incident on the interface at $z = 0$. Its polarization is assumed arbitrary. For the material interface to be reflectionless the following relationships between the properties of the two anisotropic media are necessary

$$\epsilon_1 = \epsilon_2, \quad \mu_1 = \mu_2, \tag{3.15}$$

and

$$s_{1x} = s_{2x}, \quad s_{1y} = s_{2y}. \tag{3.16}$$

Equation (3.16) can be rewritten in terms of the elements of the tensors $\mathbf{\Lambda}_1$ and $\mathbf{\Lambda}_2$, making use of (3.11). The relations are easily obtained

$$\frac{a_{1x}}{a_{2x}} = \frac{a_{1y}}{a_{2y}} = \frac{a_{2z}}{a_{1z}}. \tag{3.17}$$

The use of this result in the construction of absorbing sponge layers for numerical grid truncation is discussed next.

d. *Construction of 2D TM Layers*

Consider a rectangular domain, Ω, in a linear, homogeneous, isotropic medium of permittivity ϵ and permeability μ, and the electromagnetic field with TM polarization. To absorb outgoing waves we surround the Ω by layers that dissipate the waves propagating through them. If sufficient field attenuation is effected by these absorbers, zero field values may be assumed at their outer border, thus allowing for simple Dirichlet boundary conditions to be imposed at the ends of the domain of numerical computation without giving rise to spurious

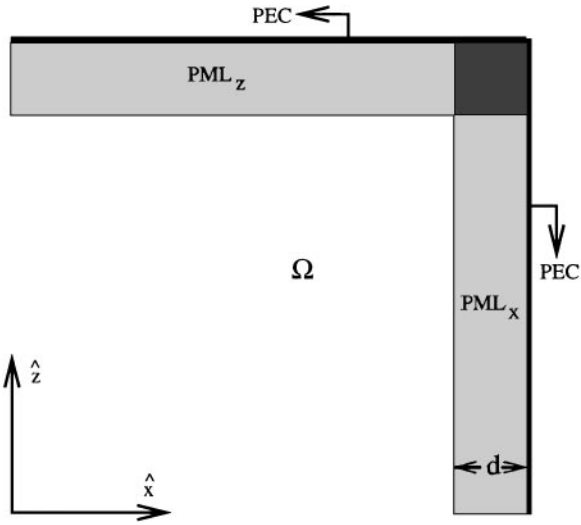

FIG. 3. The dark corner region is designated PML_{zx}.

(nonphysical) reflections. Figure 3 depicts the corner region of the domain Ω (in the x–z plane) surrounded with a sponge layer of thickness d. In two dimensions we distinguish two types of such layers: edge-layers and corner-layers.

Edge-layer. These are placed on the four edges of the rectangular computational domain. The layers labeled PML_x and PML_z in Fig. 3 fall in this category. Consider layer PML_z. Let Medium 1 be the medium inside Ω. Thus, $\epsilon_1 = \epsilon$, $\mu_1 = \mu$, and $a_{1x} = a_{1y} = a_{1z} = 1$. Let Medium 2 be the layer PML_z. According to the results in the previous section, layer PML_z will be perfectly matched to the interior medium if $\epsilon_2 = \epsilon$, $\mu_2 = \mu$ and, from (3.17),

$$a_{2x} = a_{2y} = w_z, \quad a_{2z} = w_z^{-1} \tag{3.18}$$

or, in matrix form,

$$[\Lambda^{(z)}] = \text{diag}\{w_z, w_z, w_z^{-1}\}. \tag{3.19}$$

Note that w_z is not determined at this point. Using (3.11) in (3.14), the wave number in the $\hat{z}$ direction inside layer PML_z has the form

$$k_{2z} = \omega\sqrt{\mu\epsilon}\sqrt{a_{2x}a_{2y}}\cos\theta = \omega\sqrt{\mu\epsilon}w_z\cos\theta. \tag{3.20}$$

However, as stated earlier, it is desirable to equally attenuate waves of all frequencies as they propagate through this edge-layer. Thus, the choice

$$s_{2z} = w_z = 1 + \frac{w_z''}{i\omega} \tag{3.21}$$

leads to a wave variation in the $\hat{z}$ direction inside the PML_z of the form

$$e^{-ik_{2z}z} = e^{-i\omega\sqrt{\mu\epsilon}z\cos\theta}e^{-w_z''\sqrt{\mu\epsilon}z\cos\theta}. \tag{3.22}$$

From the second term on the right-hand side of this last equation it becomes clear that the wave is attenuated in the $\hat{z}$ direction at a rate controlled by w_z''. Equation (3.22) allows us to pick the layer parameters so that the PEC backing reflects a desired amount back into the interior domain. If E_0 is the amplitude of the outgoing wave impinging upon the PML_z layer then the field that returns to the interior is

$$R \sim E_0 e^{-2dw_z''\sqrt{\mu\epsilon}\cos\theta}, \tag{3.23}$$

where d is the width of the layer. Appropriately choosing d and w_z'' results in R being as small as desired. Finally, taking into account the fact that the elements of the scaling matrix $[G]$ for this edge-PML are (from (3.9)) $g_{2x} = g_{2y} = 1$ and $g_{2z} = w_z$, Maxwell's curl equations for TM-polarized fields (H_x, H_z, and E_y) inside PML_z are written in component form as

$$\begin{aligned} i\omega\mu w_z H_x &= -(\nabla \times \mathbf{E})_x \\ i\omega\mu H_z &= -w_z(\nabla \times \mathbf{E})_z \\ i\omega\epsilon w_z E_y &= (\nabla \times \mathbf{H})_y, \end{aligned} \tag{3.24}$$

where $(\nabla \times \mathbf{F})_q$ denotes the $\hat{q}$ component of the curl of $\mathbf{F}$.

Use of (3.21) in (3.24) followed by an inverse Fourier transform results in the time-dependent form of the sponge layer equations (assuming that all fields are zero for $t \leq 0$)

$$\begin{aligned} \mu\frac{\partial H_x}{\partial t} + \mu w_z'' H_x &= -(\nabla \times \mathbf{E})_x \\ \mu\frac{\partial H_z}{\partial t} &= -(\nabla \times \mathbf{E})_z - w_z''\int_0^t (\nabla \times \mathbf{E})_z\, dt' \\ \epsilon\frac{\partial E_y}{\partial t} + \epsilon w_z'' E_y &= (\nabla \times \mathbf{H})_y. \end{aligned} \tag{3.25}$$

Clearly, the first and third equations in (3.25) have the standard form for the wave propagation in a lossy medium with electric conductivity $\sigma = \epsilon w_z''$ and magentic conductivity $\sigma^* = \mu w_z''$. The second equation in (3.25) is different in the sense that a time integral of the $\hat{z}$ component of the curl of the electric field appears on the right-hand side.This term is interpreted as a time and field-dependent source term.

The remaining three edge-layers are similarly constructed.

Corner-layer. These are placed at the four corners of the 2D rectangular domain. Figure 3 depicts one of them as PML_{zx}. The PML_{zx} must be constructed in such a way that it is matched to both edge-layers, PML_z and PML_x. In view of (3.17) and the fact that the $[\Lambda]$-matrices of the PML_x and PML_z layers are, respectively, $\mathrm{diag}\{w_x^{-1}, w_x, w_x\}$ and $\mathrm{diag}\{w_z, w_z, w_z^{-1}\}$, this corner-layer should have parameters ϵ and μ, and elements of its $[\Lambda]$-matrix should satisfy the relations

$$\begin{aligned} \frac{w_z}{a_y} = \frac{w_z^{-1}}{a_z} &= \frac{a_x}{w_z} \\ \frac{w_x^{-1}}{a_x} = \frac{w_x}{a_y} &= \frac{a_z}{w_x}. \end{aligned} \tag{3.26}$$

It is straightforward to show that these relations lead to the following $[\Lambda]$-matrix for this

corner-PML,

$$[\Lambda^{(zx)}] = \mathrm{diag}\left\{\frac{w_z}{w_x}, w_z w_x, \frac{w_x}{w_z}\right\}, \tag{3.27}$$

which may also be written in the more convenient form,

$$[\Lambda^{(zx)}] = [\Lambda^{(z)}][\Lambda^{(x)}]. \tag{3.28}$$

From (3.11), the s parameters for the PML_{zx} are easily found to be $s_x = w_x$, $s_y = 1$, and $s_z = w_z$. Considering that w_z and w_x have already been constructed according to (3.21), the expressions for k_z and k_x in (3.14) make it clear that attenuation in both $\hat{z}$ and $\hat{x}$ directions occurs as the wave propagates through this corner-layer. Finally, using the aforementioned values of s parameters and the fact that $g_x = w_x$, $g_y = 1$, and $g_z = w_z$, Maxwell's equations (TM polarization) inside the PML_{zx} take the form

$$\begin{aligned} i\omega\mu w_z H_x &= -w_x(\nabla \times \mathbf{E})_x \\ i\omega\mu w_x H_z &= -w_z(\nabla \times \mathbf{E})_z \\ i\omega\epsilon w_z w_x E_y &= (\nabla \times \mathbf{H})_y. \end{aligned} \tag{3.29}$$

In view of the fact that

$$w_x w_z = \left(1 + \frac{w_x''}{i\omega}\right)\left(1 + \frac{w_z''}{i\omega}\right) = 1 + \frac{w_x'' + w_z''}{i\omega} + \frac{w_x'' w_z''}{(i\omega)^2}, \tag{3.30}$$

the time-dependent form of (3.29) is

$$\begin{aligned} \mu\frac{\partial H_x}{\partial t} + \mu w_z'' H_x &= -(\nabla \times \mathbf{E})_x - w_x'' \int_0^t (\nabla \times \mathbf{E})_x \, dt' \\ \mu\frac{\partial H_z}{\partial t} + \mu w_x'' H_z &= -(\nabla \times \mathbf{E})_z - w_z'' \int_0^t (\nabla \times \mathbf{E})_z \, dt' \\ \epsilon\frac{\partial E_y}{\partial t} + \epsilon(w_x'' + w_z'')E_y + \epsilon w_x'' w_z'' \int_0^t E_y \, dt' &= (\nabla \times \mathbf{H})_y. \end{aligned} \tag{3.31}$$

There are now three source terms present. The ones in the first and second equations in (3.31) are similar with the ones present in the edge-layer equations in the sense that they involve time integrals of the specific component of the curl of the electric field. The source term in the third equation in (3.31) is slightly different. It involves the time integral of the corresponding electric field component.

The remaining three corner-layers are similarly constructed.

e. *Discretization*

The usefulness of the proposed sponge layer lies mainly on the fact that the frequency-domain formulation (3.24) and (3.29) lead to convenient implementation of absorbers for grid truncation in discrete, transient wave simulations, **without** the requirement for splitting of the field components. Only the discrete forms for time derivatives and time integrations are discussed since discrete forms for the spatial derivatives are dependent on the choice of placement of the field components on the numerical grid and, provided they are

effected according to the various popular stable schemes, are irrelevant to the unsplit-field formulation that is the focus of this work. In this manner, spectral, fourth-, sixth-, etc., order accurate methods, or spectral methods on rectangular grids can be used. All extra terms are discretized to the order of accuracy of the time-marching scheme (2.1). Therefore, the accuracy of the discrete sponge layer equations is $O(\Delta t^2) + O(\Delta^\rho)$, where $\rho = 2$ or 4 is the order of accuracy of the spatial stencil.

Edge-layer. Consider the layer described by (3.25). Using the $O(\Delta t^2)$ accurate trapezoidal rule for the numerical calculation of this source term one obtains

$$\int_0^{n\Delta t} (\nabla \times \mathbf{E})_z dt' = \sum_{m=0}^{n-1} (\nabla \times \mathbf{E})_z^{(m)} \Delta t + \frac{1}{2} (\nabla \times \mathbf{E})_z^{(n)} \Delta t, \tag{3.32}$$

where the superscript $^{(q)}$ notation is used to indicate that the specific quantity is calculated at time $t = q\Delta t$. Introducing the quantity

$$F_z^{(n)} = \sum_{m=0}^{n} (\nabla \times \mathbf{E})_z^{(m)} \tag{3.33}$$

and using standard central differencing for the approximation of the time derivative, the semi-discrete form of (3.25) is obtained in view of (3.22) as

$$H_z^{(n+1/2)} = H_z^{(n-1/2)} - \frac{\Delta t}{\mu} \left(1 + \frac{w_z''}{2} \Delta t\right) (\nabla \times \mathbf{E})_z^{(n)} - \frac{w_z'' \Delta t^2}{\mu} F_z^{(n-1)}. \tag{3.34}$$

Clearly, once H_z has been updated, F_z should be updated also using

$$F_z^{(n)} = F_z^{(n-1)} + (\nabla \times \mathbf{E})_z^{(n)}. \tag{3.35}$$

The time-dependent equations for the edge-layer in the $\hat{x}$ direction and their subsequent semi-discrete approximations are developed in a similar fashion. For each layer one time-dependent source term is introduced. Its update involves the simple operation indicated in (3.35). Time averaging the terms $w_z'' H_x$, and $w_z'' E_y$, along with (3.32)–(3.34), results in an overall $O(\Delta t^2)$ accurate discretization of (3.25).

Corner-layer. Next, consider the layer described by (3.29). Using the notation

$$\begin{aligned} \alpha_q^+ &= 1 + \frac{\Delta t}{2} w_q'' \\ \alpha_q^- &= 1 - \frac{\Delta t}{2} w_q'', \end{aligned} \tag{3.36}$$

the relevant semi-discrete forms of the first and second equations in (3.29) are

$$\begin{aligned} H_x^{(n+1/2)} &= \frac{\alpha_z^-}{\alpha_z^+} H_x^{(n-1/2)} - \frac{\Delta t \alpha_x^+}{\mu \alpha_z^+} (\nabla \times \mathbf{E})_x^{(n)} - \frac{w_x'' \Delta t^2}{\mu \alpha_z^+} \sum_{m=0}^{n-1} (\nabla \times \mathbf{E})_x^{(m)} \\ H_z^{(n+1/2)} &= \frac{\alpha_x^-}{\alpha_x^+} H_z^{(n-1/2)} - \frac{\Delta t \alpha_z^+}{\mu \alpha_x^+} (\nabla \times \mathbf{E})_z^{(n)} - \frac{w_z'' \Delta t^2}{\mu \alpha_x^+} \sum_{m=0}^{n-1} (\nabla \times \mathbf{E})_z^{(m)}. \end{aligned} \tag{3.37}$$

Again, $O(\Delta t^2)$ accuracy is maintained.

The time discretization of the source term in the third equation in (3.31) at $t = (n+\frac{1}{2})\Delta t$ will involve the integral

$$\int_0^{(n+1/2)\Delta t} E_y dt'. \tag{3.38}$$

Using the trapezoidal rule for the numerical calculation of this integral and in view of the fact that the electric field is sampled in time at points $i\Delta t$, $i = 1, 2, \ldots$, one obtains

$$\int_0^{(n+1/2)\Delta t} E_y dt' = \sum_{m=0}^{n} E_y^{(m)} \Delta t. \tag{3.39}$$

This last expression, along with the definition of the quantities

$$\begin{aligned} \gamma_{pq}^{+} &= 1 + \frac{\Delta t}{2}(w_p'' + w_q'') \\ \gamma_{pq}^{-} &= 1 - \frac{\Delta t}{2}(w_p'' + w_q''), \end{aligned} \tag{3.40}$$

leads to the following $O(\Delta t^2)$ accurate form for the semi-discrete approximation of the third equation in (3.31):

$$E_y^{(n+1)} = \frac{\gamma_{zx}^{-}}{\gamma_{zx}^{+}} E_y^{(n)} + \frac{\Delta t}{\epsilon \gamma_{zx}^{+}} (\nabla \times \mathbf{H})_y^{(n+1/2)} - \frac{w_x'' w_z'' \Delta t^2}{\gamma_{zx}^{+}} \sum_{m=0}^{n} E_y^{(m)}. \tag{3.41}$$

The time-dependent equations for the other three corner-PMLs and their subsequent semidiscrete approximations are developed in a similar fashion.

f. *Well-Posedness*

We now show that the extra terms appearing in (3.25) and (3.31) are lower order (undifferentiated) perturbations of the strongly well-posed problem (2.1). Then, via Theorem (4.32) of [11], our sponge layer equations are also **strongly well-posed**.

Edge-layer. We begin by rewriting (3.24) in two dimensions as

$$\begin{aligned} i\omega B_x &= \frac{\partial E_y}{\partial z} \\ i\omega B_z &= -\frac{\partial E_y}{\partial x} \\ i\omega D_y &= \frac{\partial H_z}{\partial x} + \frac{\partial H_x}{\partial z}, \end{aligned} \tag{3.42}$$

closed with constitutive relations

$$\begin{aligned} B_x &= \mu \left(1 + \frac{w_z''}{i\omega}\right) H_x \\ B_z &= \mu \frac{i\omega}{w_z'' + i\omega} H_z \\ D_y &= \epsilon \left(1 + \frac{w_z''}{i\omega}\right) E_y. \end{aligned} \tag{3.43}$$

Using the inverse Fourier transform in (3.42)–(3.43), we obtain the edge-PML equations in the time-domain

$$\begin{aligned}\frac{\partial B_x}{\partial t} &= \frac{\partial E_y}{\partial z}\\ \frac{\partial B_z}{\partial t} &= -\frac{\partial E_y}{\partial x}\\ \frac{\partial D_y}{\partial t} &= -\frac{\partial H_z}{\partial x} + \frac{\partial H_x}{\partial z},\end{aligned} \tag{3.44}$$

closed with the hereditary constitutive relations

$$\begin{aligned}B_x &= \mu H_x + \mu w_z'' \int_0^t H_x\, dt'\\ B_z &= \mu \int_0^t e^{-w_z''(t-t')} \frac{\partial H_z}{\partial t'}\, dt'\\ D_y &= \epsilon E_y + \epsilon w_z'' \int_0^t E_y\, dt'.\end{aligned} \tag{3.45}$$

Now, the first and third equations in (3.45) just indicate that there are magnetic and electric losses in the tangential to the layer directions, while the second equation indicates memory of the time rate of change of the normal to the layer magnetic field. Taking the time derivative of every equation in (3.45) and subsequently applying integration by parts (assuming zero initial conditions for the fields in the layer) to the second one, we obtain

$$\begin{aligned}\frac{\partial B_x}{\partial t} &= \mu \frac{\partial H_x}{\partial t} + \mu w_z'' H_x\\ \frac{\partial B_z}{\partial t} &= \mu \frac{\partial H_z}{\partial t} - \mu w_z'' H_z + \mu w_z''^2 \int_0^t e^{-w_z''(t-t')} H_z\, dt'\\ \frac{\partial D_y}{\partial t} &= \epsilon \frac{\partial E_y}{\partial t} + \epsilon w_z'' E_y.\end{aligned} \tag{3.46}$$

Substituting (3.46) in the left-hand side of (3.44) we recover (2.1), modified by lower-order (undifferentiated) terms. Due to the equivalence of (3.44) (with (3.46)) and (3.25) we say that the extra term in (3.25) is a lower order term.

Corner-layer. System (3.29) can be put in the same form as (3.42) now closed with constitutive relations

$$\begin{aligned}B_x &= \mu \frac{w_z}{w_x} H_x\\ B_z &= \mu \frac{w_x}{w_z} H_z\\ D_y &= \epsilon w_z w_x E_y,\end{aligned} \tag{3.47}$$

where $w_{z(x)} = 1 + w''_{z(x)}/i\omega$. It easy to show that

$$\frac{w_{z(x)}}{w_{x(z)}} = 1 + \frac{w''_{z(x)}/w''_{x(z)} - 1}{1 + i\omega/w''_{x(z)}}. \tag{3.48}$$

With (3.30) and the inverse Fourier transform we obtain again (3.44) but now closed with the hereditary constitutive relations

$$\begin{aligned} B_x &= \mu H_x + \mu(w_z'' - w_x'') \int_0^t e^{-w_x''(t-t')} H_x \, dt' \\ B_z &= \mu H_z + \mu(w_x'' - w_z'') \int_0^t e^{-w_z''(t-t')} H_z \, dt' \\ \frac{\partial D_y}{\partial t} &= \epsilon \frac{\partial E_y}{\partial t} + \epsilon(w_x'' + w_z'') E_y + \epsilon w_x'' w_z'' \int_0^t E_y \, dt'. \end{aligned} \tag{3.49}$$

Substituting (3.49) in (3.44) yields again system (2.1) modified by lower order (undifferentiated) terms. It is interesting to note that when $w_x'' = w_z''$ then the magnetic aspect of (3.49) is lossless.

g. *Numerical Stability*

In Section 3f we showed that the sponge layer equations are just Maxwell's equations for a homogeneous nondispersive dielectric modified with lower-order (undifferentiated) terms. Such terms were seen to be equivalent to terms proportional to the fields or their weighted time integrals, e.g., H_x, $\int_0^t H_x dt'$, or $\int_0^t e^{-w_z''(t-t')} H_x dt'$. Also, in Section 3e we showed that these extra terms can be implemented in a way that preserves the second-order time accuracy of (2.3). Thus, upon discretization, terms like those below will modify the amplification matrix of the staggered-grid finite-differenced Maxwell equations for a homogeneous nondispersive dielectric as indicated in the order symbol:

$$\begin{aligned} &\Delta t \{H_x\}_{discrete} \sim O(\Delta t) \\ &\Delta t \left\{ \int_0^t H_x \, dt' \right\}_{discrete} \sim O(\Delta t^2) \\ &\Delta t \left\{ \int_0^t e^{-w_z''(t-t')} H_x \, dt' \right\}_{discrete} \sim O(\Delta t^2). \end{aligned} \tag{3.50}$$

As a result, in a von Neumann stability analysis, the original amplification matrix will be modified by terms that will be $O(\Delta t)$ and $O(\Delta t^2)$ uniformly in wavenumber. This will result in the **necessary and sufficient** condition (2.6) of the interior scheme to also hold for the sponge layer equations (via Theorem 6.2.6 in [26]).

In (3.25) and (3.31) the additional terms are proportional to, e.g., $\int_0^t (\nabla \times \mathbf{E})_z dt'$. However, upon discretization,

$$\Delta t \left\{ \int_0^t (\nabla \times \mathbf{E})_z dt' \right\}_{discrete} \sim O(\nu \Delta t) \tag{3.51}$$

uniformly in wavenumber; thus, (2.6) also holds for the thusly modified Maxwell equations in the sponge layer.

4. NUMERICAL EXPERIMENTS

Figure 4 depicts a circular scatterer of relative permittivity ϵ_s and radius r_s illuminated by a cylindrically spreading wave generated with the pulsed electric-current point-source $\mathbf{J}(\mathbf{x}, \mathbf{x}', t) = \hat{y}\delta(\mathbf{x} - \mathbf{x}')g(t) = \hat{y}(\delta_{i-i',j-j'}/\Delta^2)g(t)$, where (i', j') is the location of the source point $\mathbf{x}'$ on the grid, $g(t) = E_0(10 - 15\cos\omega_1 t + 6\cos\omega_2 t - \cos\omega_3 t)$ is a compact smooth function supported in $t \in [0, t_s]$, and E_0 is the maximum source amplitude. When present, the scatterer is centered on the grid, and the point source is placed so that $|x_s - x'| = 2r_s$ and $y_s = y'$. Otherwise, the source is centered on the grid and the scatterer is a phantom ($\epsilon_s = 1$). We take $t_s = 10^{-9}$ s, $\omega_m = 2\pi m/t_s$, $m = 1, 2, 3$, $\epsilon_s = 4$, $r_s = 2c_\infty t_s/3$, and $E_0 = Z_0/320$ with $Z_0 = \sqrt{\mu_0/\epsilon_0}$ being the free-space impedance.

Our scattering problem is embedded in a two-dimensional, infinite, homogeneous, lossless, dielectric with $\epsilon_r = 1$. We solve it numerically with scheme (2.3), in a finite-sized test domain Ω_C, with boundary $\partial\Omega_C$, itself embedded inside a much larger reference domain Ω_L with boundary $\partial\Omega_L$. Domain Ω_C is truncated by either placing on $\partial\Omega_C$ one of the local RBCs considered herein, or by surrounding Ω_C with a uniform width ($d = 4ct_s/15$) sponge layer Ω_S bounded by $\partial\Omega_C$ and $\partial\Omega_S$. On $\partial\Omega_S$ and $\partial\Omega_L$ we implement a PEC boundary condition using images [21], thus preserving the interior scheme spatial order of accuracy there. The reference domain boundary is placed sufficiently far from $\partial\Omega_C$ to provide causal isolation between all points in the test domain and reflections generated at $\partial\Omega_L$ over a given computation time interval $[0, T = 3t_s]$. The physical size of Ω_C is $L^2 = 25(c_\infty t_s)^2/9$.

To test and compare the boundary treatments considered herein we compute the error

$$e(n\Delta t) = \|EY^{\Omega_C}(\cdot, \cdot, n\Delta t) - EY^{\Omega_L}(\cdot, \cdot, n\Delta t)\|_2; n \in [0, T/\Delta t], \tag{4.1}$$

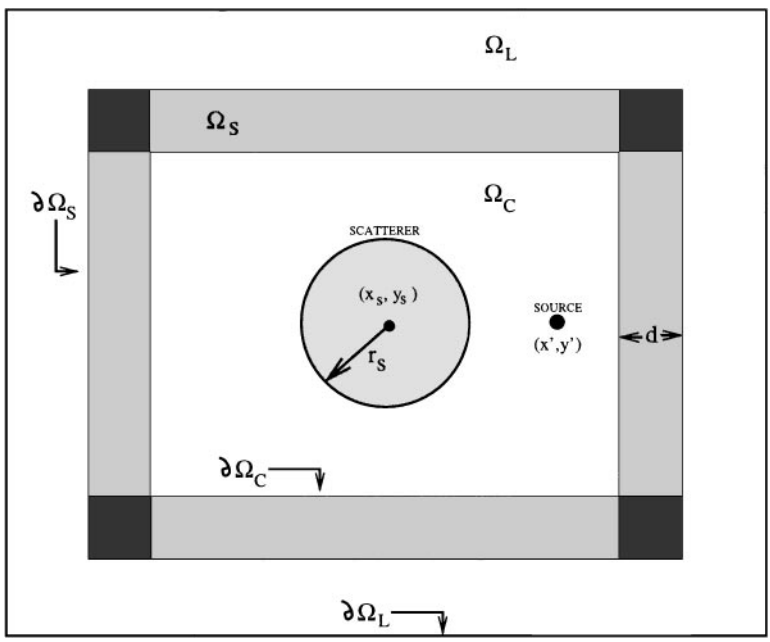

FIG. 4. Geometry used in the numerical experiments.

introduced at each timestep n by the artificial truncation of Ω_C. In (4.1), EY^{Ω_C,Ω_L} is the discrete electric field in the appropriate domain indicated by the superscript, and the L_2 norm is taken over the interior of Ω_C. Note that $e(n\Delta t) = 0$ for $n \in [0, T_{int}/\Delta t]$, where T_{int} is the least time required for the outgoing waves to start interacting with $\partial\Omega_C$. The definition (4.1) is a measure of how well the artificial truncation approximates the true "physics" at the boundary which dictate that there should be no boundary felt by the outgoing waves; were the ABC ideal, this measure would be identically equal to zero for *all* n. We also compute $\|e(\cdot)\|_\ell$, $\ell = 1, 2, \infty$, for $n \in [0, T/\Delta t]$ on a sequence of grids generated by successively halving Δ while keeping the CFL number constant at $\nu = 0.1$. We assume $\|e(\cdot)\|_\ell \sim O(\Delta^r)$ and compute the exponent r from the numerical results. On the coarsest grid $\Delta = 0.02$, while $\Delta = 0.00125$ on the finest grid.

The sponge-layer/free-space interface is reflectionless for analytic waves; however, discrete waves may partially reflect from it. For this reason, w_x'' and w_z'' are implemented as the functions $\sigma_{max}(x/d)^p$, where x is distance from the sponge-layer/free-space interface along the normal into the layer and p is the order of variation. We choose parameters so that (3.23) for $w_x'' = w_z'' = \sigma_{max} = 28.125/(Z_0 c t_s)$ gives 10^{-q} for the R (3.23) due to the PEC backing at normal incidence. For the simulations we used $q = 5$ and $p = 2$. The value for d used herein corresponds to a layer eight grid cells wide at $\Delta = 0.01$. An important parameter in the sponge layer is the relaxation time $\tau = \epsilon_0/\sigma_{max}$. The time-resolution parameter in the sponge layer is $h = \Delta t/\tau = 93.75\nu\Delta$ which, for the values given above, satisfies $0.0117 \le h \le 0.1875$. Thus, the time-discretization is accurately approximating the effect of the small relaxation timescale in the sponge layer [23]. The parameters in the second- and third-order Higdon operators were set to provide perfect annihilation of plane waves impinging normally on $\partial\Omega_C$, while enforcing each discrete operator to be implemented with the second-order-accurate box scheme [13]. Once chosen, the physical width of the sponge layer and all other problem dimensions and parameters were kept invariant during the mesh refinement studies.

We first give results for a radiation problem where the scatterer is absent and the source is centered in the test and comparison grids. Figure 5 compares the "physical" errors (4.1) introduced by the boundary truncations. We see the sponge layer to be superior to the other methods by more than three orders of magnitude. It is interesting to note that the third-order Higdon operator performs poorly for late times. This is expected, as it is badly behaved at zero-frequency, where it possesses a generalized eigenvalue that produces instability [13]. The zero-frequency in our problem is introduced by the fact that in two dimensions a passing wavefront leaves behind it an algebraically decaying residue that persists for long times. Hence, after the main pulse passes through $\partial\Omega_C$, the remaining slowly decaying residue acts as a zero-frequency forcing of the boundary operator. Figure 6 summarizes the results of the mesh refinement. Again, the superiority of the sponge layer is evident. The slope of the dash-dot line on the graph is roughly 4. The norms $\|e(\cdot)\|_\ell$, $\ell = 1, \infty$, gave similar results. The deterioration of the third-order condition with grid refinement confirms our explanation of its poor performance. Figures 7 and 8 present results similar to those described in the previous paragraph but for the scattering problem described above. The superiority of the sponge layer is again evident. The slope of the dash-dot line on Fig. 8 is roughly 3.5. All other time norms of (4.1) gave similar results. It must be noted that the second-order Higdon operator and the sponge layer are robust with respect to changes in the physical problem being modeled (from radiation to scattering), while this seems not to be the case for the third-order operator.

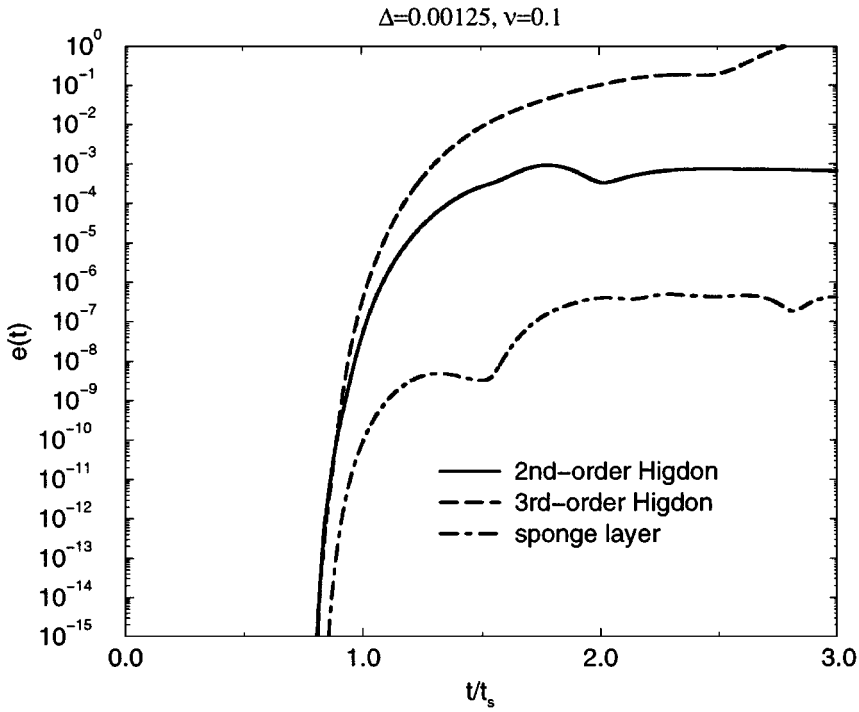

FIG. 5. Time evolution of the error (4.1) for the radiation problem.

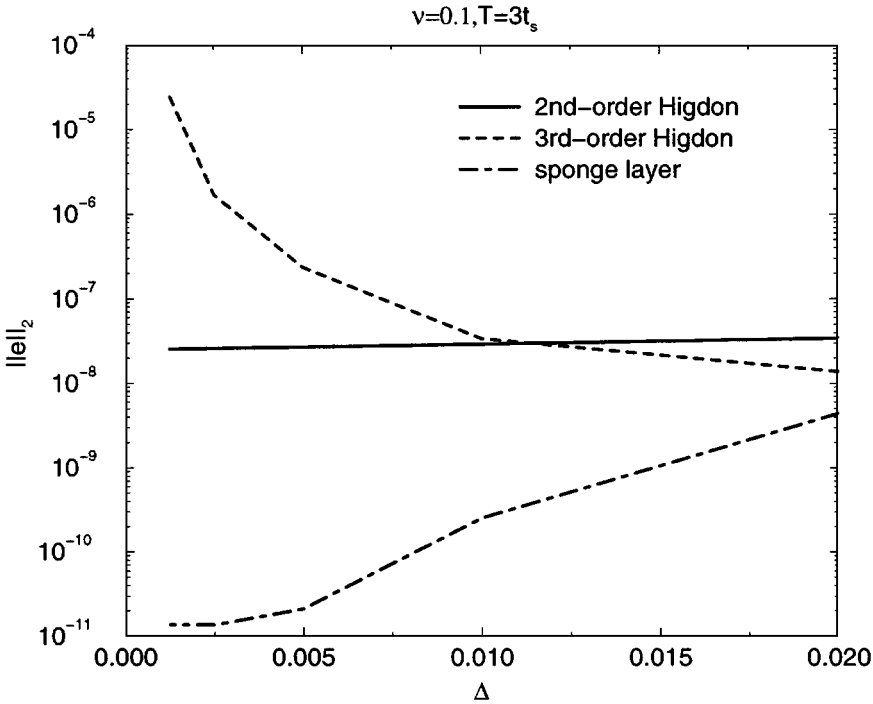

FIG. 6. Convergence of the reflection property in the L_2 norm for the radiation problem.

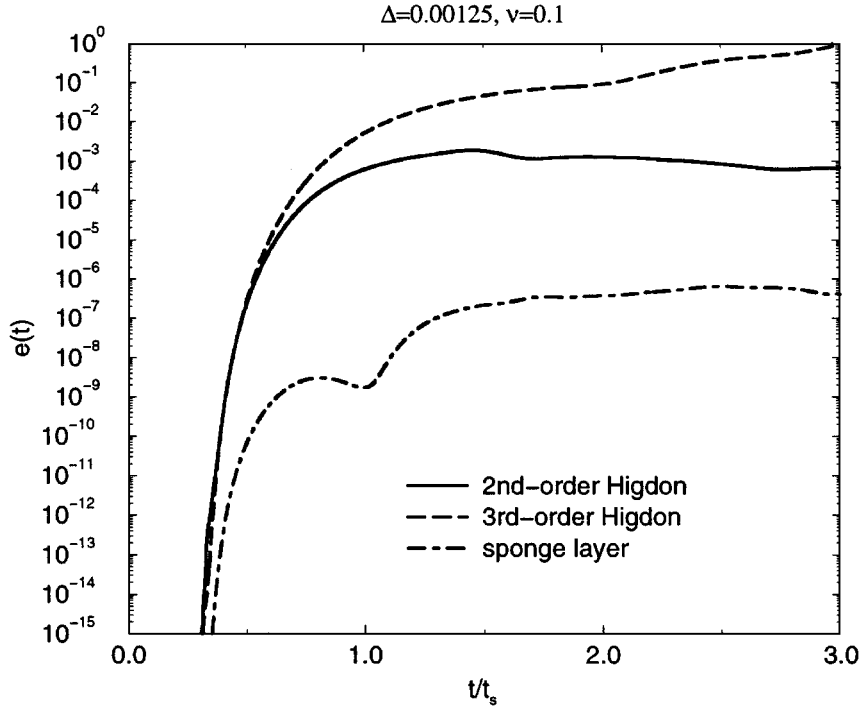

FIG. 7. Time evolution of the error (4.1) for the scattering problem.

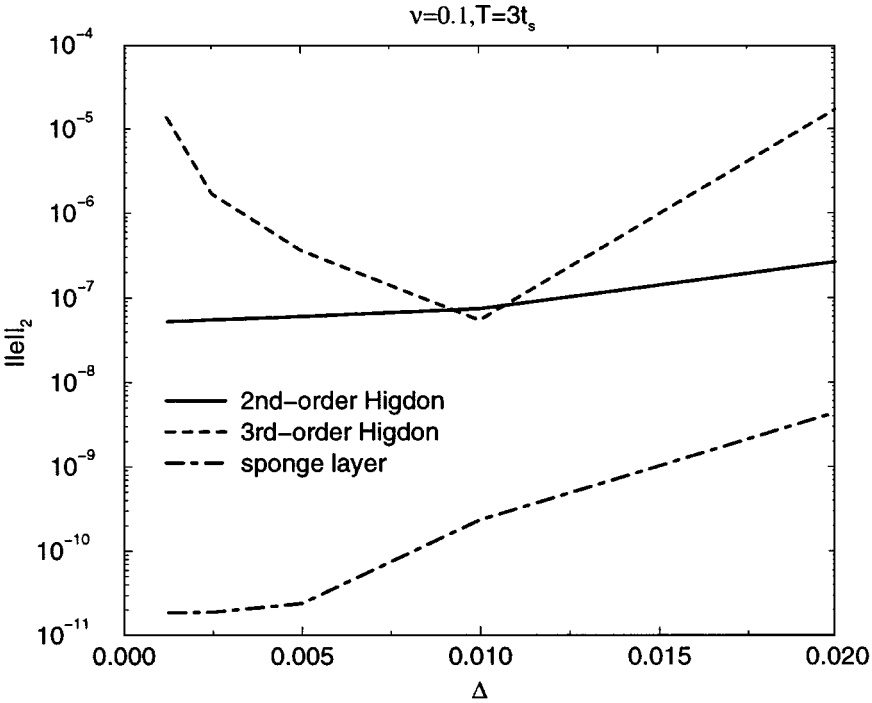

FIG. 8. Convergence of the reflection properties in the L_2 norm for the scattering problem.

In order to show that the numerical results obtained with our strongly well-posed approach are similar to those obtained with the ill-posed Berenger system we have used an existing (2,2) code that implements [2], to solve the scattering problem depicted in Fig. 4. The Berenger layer width was the same as the corresponding parameter in the sponge layer above. The maximum conductivities in the Berenger and sponge layers were tuned to give the least reflection with $\Delta = 0.01$ and $\nu = 0.5$. Figure 9 shows a comparison between the approach used herein and the Berenger PML for $\alpha = 1$, $\beta = 0$ in (2.3). Figure 10 shows that the reflectionless property of both approaches is approached at the rate of convergence of the interior scheme (here equal to 2). It is interesting to note that our sponge layer approach performs better on the coarser grid. Finally, we note that a comparison of the computational burdens incurred by our sponge layer and by that of Berenger has been presented in [29]. The conclusions of that comparison hold also for the higher order schemes discussed here, since the use of either Berenger's PML or the unsplit-field sponge layer does not impact the stencil used for the numerical spatial differentiation of the fields. Thus, the savings on computational resources and labor depend solely on the number of the extra degrees of freedom introduced by each of the two implementations and the number of arithmetic operations required for the update of all degrees of freedom per time step. As pointed out in [29], assuming a cubical computational domain of N cells per side, the sponge layer implementation results in memory savings of $\sim$25% over Berenger's PML. These savings are primarily contributed by the faces and edges of the domain, where the unsplit-field implementation requires only two and four, respectively, extra degrees of freedom, compared to six for both cases for Berenger's PML. These savings in computer memory are

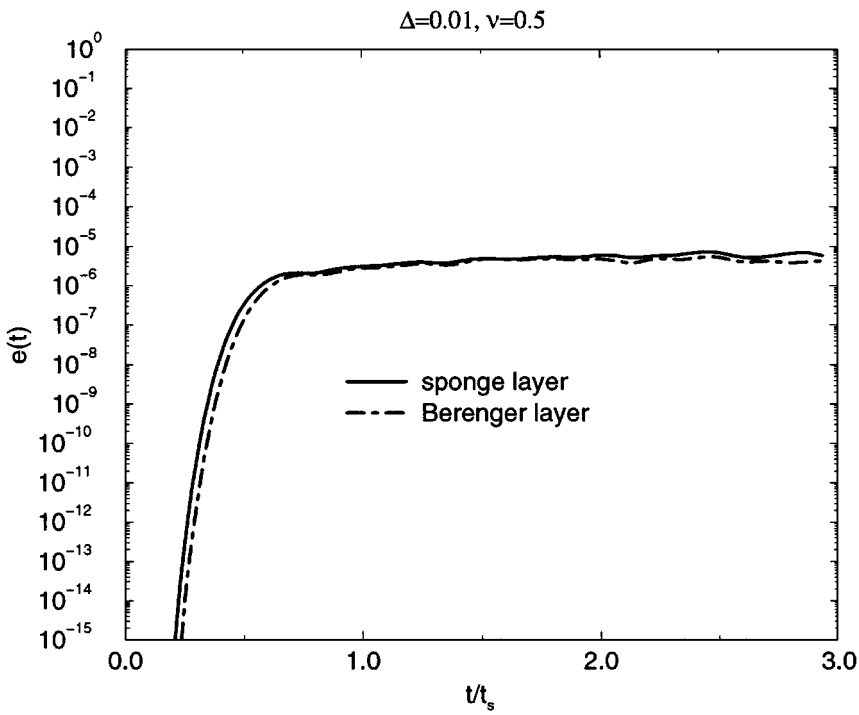

FIG. 9. Time evolution of the error (4.1) for the scattering problem.

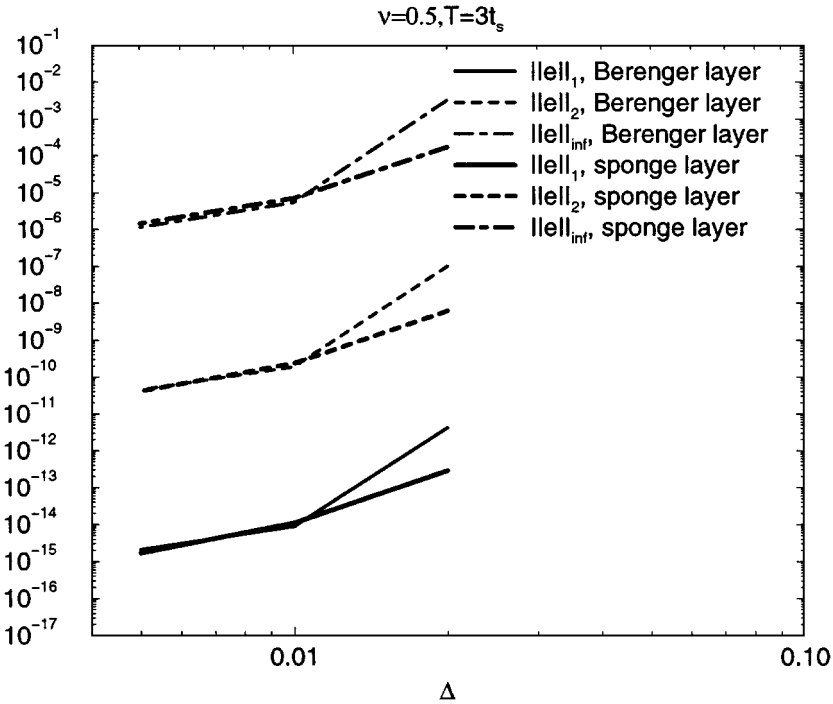

FIG. 10. Convergence of the reflection properties in the L_1, L_2, and L_∞ norms for the scattering problem.

accompanied by a reduced CPU time since the number of both additions/subtractions and multiplications/divisions required for the update of the fields at both the perfectly matched faces and edges of the domain is larger for Berenger's PML implementation than that for the sponge layer implementation.

5. SUMMARY

We have presented a reflectionless sponge layer for the truncation of cartesian computational domains used in the numerical solution of linear hyperbolic systems arising in transient electromagnetics with high-order staggered finite differences schemes. The sponge layer is independent of the spatial discretization and our numerical experiments demonstrated its utility when the equations are solved with a particular (2, 4) staggered nondissipative scheme. We also showed that our approach to absorbing boundary conditions involves systems of equations that possess the mathematical and numerical properties of the equations that are to be solved in the interior. We have also compared the performance of the layer relative to the performance of classical local radiation boundary conditions adapted to the high-order stencil. The sponge layer is superior to these local RBCs from the point of view that the "physical" reflection produced by it converges to zero at the rate of the interior scheme. Our sponge layer allows for the local nature of finite-difference discretizations of Maxwell's equations to be maintained at the boundary thus allowing for ease of parallelization.

ACKNOWLEDGMENT AND DISCLAIMER

The first author thanks Professors K. S. Nikita and N. G. Uzunoglu of the Electroscience Division, Department of Electrical Engineering, National Technical University of Athens, Greece for their hospitality during the initial writing of this paper. Peter G. Petropoulos was sponsored by the Air Force Office of Scientific Research, Air Force Materials Command, USAF, under Grant F49620-95-1-0014. The views and conclusions contained herein are those of the authors and should not be interpreted as necessarily representing the official policies or endorsements, either expressed or implied, of the Air Force Office of Scientific Research or the U.S. Government.

REFERENCES

1. S. Abarbanel and D. Gottlieb, A mathematical analysis of the PML method, *J. Comput. Phys.* **134**, 357 (1997).
2. J.-P. Berenger, A perfectly matched layer for the absorption of electromagnetic waves, *J. Comput. Phys.* **114**, 185 (1994).
3. W. C. Chew and W. H. Weedon, A 3-D perfectly matched medium from modified Maxwell's equations with stretched coordinates, *Micro. Opt. Tech. Lett.* **7**(13), 599 (1994).
4. T. Deveze, L. Beaulieu, and W. Tabbara, An absorbing boundary condition for the fourth-order FDTD scheme, in *IEEE-APS International Symposium Proceedings, Chicago, IL, 1992*, p. 342.
5. T. H. Duong and P. Joly, A principle of images for absorbing boundary conditions, *Num. Meth. Part. Diff. Equations* **10**, 411 (1994).
6. J. Fang, *Time Domain Finite Difference Computations for Maxwell's Equations*, Ph.D. dissertation, Dept. of Elec. Eng., University of California, Berkeley, CA, 1989 .
7. D. Givoli, Non-reflecting boundary conditions, *J. Comput. Phys.* **94**, 1 (1991).
8. D. Givoli and D. Cohen, Nonreflecting boundary conditions based on Kirchhoff-type Formulae, *J. Comput. Phys.* **117**(1), 102 (1995).
9. M. J. Grote and J. B. Keller, Nonreflecting boundary conditions for time-dependent scattering, *J. Comput. Phys.* **127**(1), 52 (1996).
10. D. Gottlieb and B. Yang, Comparisons of staggered and non-staggered schemes for Maxwell's equations, in *Proceedings, 12th Annual Review of Progress in Applied Computational Electromagnetics, 1996*.
11. B. Gustafson, H. O. Kreiss, and J. Oliger, *Time Dependent Problems and Difference Methods* (Wiley, New York, 1995).
12. B. Gustafsson, Far-field boundary conditions for time-dependent hyperbolic systems, *SIAM J. on Scientific and Statistical Computing* **9**(5), 812 (1988).
13. R. L. Higdon, Radiation boundary conditions for elastic wave propagation, *SIAM J. Numer. Anal.* **27**(4), 831 (1990).
14. M. Israeli and S. A. Orszag, Approximation of radiation boundary conditions, *J. Comput. Phys.* **41**, 115 (1981).
15. J. D. Jackson, *Classical Electrodynamics*, 2nd ed. (Wiley, New York, 1975).
16. S. Karni, Far-field filtering operators for suppression of reflections from artificial boundaries, *SIAM J. Numer. Anal.* **33**(3), 1014 (1996).
17. A. R. Levander, Use of the telegraphy equation to improve absorbing boundary efficiency for fourth-order acoustic wave finite differences schemes, *Bull. Seism. Soc. Am.* **75**(6), 1847 (1985).
18. Y. Liu, Fourier analysis of numerical algorithms for the Maxwell equations, *J. Comput. Phys.* **124**, 396 (1996).
19. A. Nachman, A brief perspective on computational electromagnetics, *J. Comput. Phys.* **126**, 237 (1996).
20. A. C. Newel and J. V. Moloney, *Nonlinear Optics* (Addison–Wesley, Reading, MA, 1992).
21. P. G. Petropoulos, Phase error control for FD-TD methods of second and fourth order accuracy, *IEEE Trans. on Antennas and Propagation* **42**, 859 (1994).
22. P. G. Petropoulos, The wave hierarchy for propagation in relaxing dielectrics, *Wave Motion* **21**, 253 (1995). [The computation of linear dispersive electromagnetic waves, *ACES J.* **11**, 8(1996)]
23. P. G. Petropoulos, Analysis of exponential time-differencing for FD-TD in lossy dielectrics, *IEEE Trans. Antennas Propag.* **45**(6), 1054 (1997).

24. Z. S. Sacks, D. M. Kingsland, R. Lee, and J.-F. Lee, A perfectly matched anisotropic absorber for use as an absorbing boundary condition, *IEEE Trans. on Antennas and Propagation* **43**(12), 1460 (1995).
25. A. Taflove, *Computational Electrodynamics: The Finite-Difference Time-Domain Method* (Artech House, Boston, 1995).
26. J. W. Thomas, *Numerical Partial Differential Equations-Finite Difference Methods* (New York: Springer-Verlag, 1995).
27. S. V. Tsynkov, An application of nonlocal external conditions to viscous flow computations, *J. Comput. Phys.* **116**(2), 212 (1995).
28. K. S. Yee, Numerical solution of initial boundary value problems involving Maxwell's equations in isotropic media, *IEEE Trans. Antennas Propagat.* **14**, 302 (1966).
29. L. Zhao and A. C. Cangellaris, GT-PML: Generalized theory of perfectly matched layers and its application to the reflectionless truncation of finite-difference time-domain grids, *IEEE Trans. Microwave Theory Tech.* **44**(12), 2555 (1996).